

Cite this: *Chem. Sci.*, 2017, 8, 2073

# Antimony-ligated dysprosium single-molecule magnets as catalysts for stibine dehydrocoupling†

Thomas Pugh, Nicholas F. Chilton\* and Richard A. Layfield\*

Single-molecule magnets (SMMs) are coordination compounds that exhibit magnetic bistability below a characteristic blocking temperature. Research in this field continues to evolve from its fundamental foundations towards applications of SMMs in information storage and spintronic devices. Synthetic chemistry plays a crucial role in targeting the properties that could ultimately produce SMMs with technological potential. The ligands in SMMs are invariably based on non-metals; we now report a series of dysprosium SMMs (in addition to their magnetically dilute analogues embedded in yttrium matrices) that contain ligands with the metalloid element antimony as the donor atom, *i.e.*  $[(\eta^5\text{-Cp}'_2\text{Dy})(\mu\text{-Sb}(\text{H})\text{Mes})_3]$  (**1-Dy**) and  $[(\eta^5\text{-Cp}'_2\text{Dy})_3(\mu\text{-Sb}(\text{H})\text{Mes})_3\text{Sb}]$  (**2-Dy**), which contain the stibinide ligand  $[\text{Mes}(\text{H})\text{Sb}]^-$  and the unusual Zintl-like ligand  $[\text{Sb}_4\text{Mes}_3]^{3-}$ , respectively (Cp' = methylcyclopentadienyl; Mes = mesityl). The zero-field anisotropy barriers in **1-Dy** and **2-Dy** are  $U_{\text{eff}} = 345 \text{ cm}^{-1}$  and  $270 \text{ cm}^{-1}$ , respectively. Stabilization of the antimony-ligated SMMs is contingent upon careful control of reaction time and temperature. With longer reaction times and higher temperatures, the stibine pro-ligands are catalytically dehydrocoupled by the rare-earth precursor complexes. NMR spectroscopic studies of the yttrium-catalysed dehydrocoupling reactions reveal that **1-Y** and **2-Y** are formed during the catalytic cycle. By implication, **1-Dy** and **2-Dy** should also be catalytic intermediates, hence the nature of these complexes as SMMs in the solid-state and as catalysts in solution introduces a strategy whereby new molecular magnets can be identified by intercepting species formed during catalytic reactions.

Received 6th October 2016  
Accepted 21st November 2016

DOI: 10.1039/c6sc04465d

www.rsc.org/chemicalscience

## Introduction

The synthesis of complex magnetic materials from simple chemical building blocks encapsulates the intrinsic fascination of molecular magnetism. Molecular magnets are typically designed using bottom-up approaches that provide access to experimental testbeds for theoretical models of magnetism, and that enable modular approaches to applications based on the properties of well-defined magnetic units. For example, carefully constructed transition metal complexes display characteristics that could lead to their implementation as molecular qubits for quantum computing.<sup>1</sup> The magnetocaloric effect, in which the entropy of a magnetic system is modulated by a magnetic field, introduces the possibility of using molecular magnets as refrigerants that function more efficiently than conventional cryogenes.<sup>2</sup> Spin-crossover materials, which have been intensively studied for many years,<sup>3</sup> have been proposed

for applications in displays, sensors and information storage devices.<sup>4</sup> Lanthanide complexes continue to play important roles in enhancing our understanding of ligand field theory,<sup>5</sup> and many such species find applications in NMR spectroscopy as shift reagents<sup>6</sup> and in magnetic resonance imaging.<sup>7</sup>

Single-molecule magnets (SMMs) are coordination compounds that can be defined by an effective energy barrier ( $U_{\text{eff}}$ ) to reversal of their magnetization.<sup>8</sup> The pioneering work on SMMs focused on exchange-coupled transition metal cage compounds,<sup>9,10</sup> and monometallic 3d complexes have recently emerged as another important class of SMM.<sup>11–13</sup> Many of the most exciting developments in single-molecule magnetism have been accounted for by the lanthanides terbium, dysprosium and erbium,<sup>14–19</sup> and lanthanide SMMs have been described with very high  $U_{\text{eff}}$  values and magnetic blocking temperatures.<sup>20–22</sup> Studies of the interactions between electrical currents and SMMs on surfaces has also led to the development of prototype molecular spintronic devices.<sup>23,24</sup>

Despite the remarkable progress with SMMs, challenges remain, including overcoming the need for liquid-helium temperatures to observe slow relaxation of the magnetization, and the need to organise and stabilise molecules on surfaces for devices to become viable. To address these challenges, novel synthetic coordination chemistry strategies are of prime importance. Ligand environments in SMMs, especially those

School of Chemistry, The University of Manchester, Oxford Road, Manchester, M13 9PL, UK. E-mail: Richard.Layfield@manchester.ac.uk; Nicholas.Chilton@manchester.ac.uk

† Electronic supplementary information (ESI) available: Synthetic details, spectroscopic characterization for all compounds, X-ray crystallography details and crystallographic information files, computational details. CCDC 1484570–1484573 and 1485316. For ESI and crystallographic data in CIF or other electronic format see DOI: 10.1039/c6sc04465d



containing lanthanides, are dominated by hard, oxygen- and nitrogen-donor atoms.<sup>8–22</sup> Targeting lanthanide SMMs with ligands in which the donor atoms have metallic character would introduce new ways of influencing the metal–ligand bonding and hence the electronic structure of the metal ion, potentially providing a way of enhancing the magnetic relaxation properties. Furthermore, using metalloid donor ligands as building blocks in SMMs could unearth new reactivity, which could itself be manipulated further for the synthesis of new molecular magnets.

## Results and discussion

We now describe two dysprosium-containing SMMs based on the metallocene building block  $\{\text{Cp}_2\text{Dy}(\text{E})_2\}$ , where E denotes a ligand with the 5p metalloid element antimony as the donor atom. We focus on the trimetallic complexes  $[(\eta^5\text{-Cp}'_2\text{Dy})\{\mu\text{-Sb}(\text{H})\text{Mes}\}]_3$  (**1-Dy**) and  $[(\eta^5\text{-Cp}'_2\text{Dy})_3\{\mu\text{-}(\text{SbMes})_3\text{Sb}\}]$  (**2-Dy**), which contain the stibinide ligand  $[\text{Mes}(\text{H})\text{Sb}]^-$  and the Zintl-like ligand  $[\text{Sb}_4\text{Mes}_3]^{3-}$ , respectively (Cp' = methylcyclopentadienyl; Mes = mesityl). Compound **1-Y** and the yttrium analogue **1-Y** were synthesized by adding three equivalents of  $\text{MesSbH}_2$  to a 3 : 3 mixture of  $\text{Cp}'_3\text{M}$  and  $n\text{BuLi}$  over 30 minutes at  $-50^\circ\text{C}$  (Scheme 1). Compounds **2-M** were synthesized in a similar fashion with four equivalents of  $\text{MesSbH}_2$ , with the reaction being warmed from  $-78^\circ\text{C}$  to room temperature overnight. Without careful control of reaction time and temperature, stibine dehydrocoupling occurs to give the 1,2-distibane  $\text{Sb}_2\text{H}_2\text{Mes}_2$  (Fig. S1†), the tetrastibetane  $\text{Sb}_4\text{Mes}_4$ ,<sup>25,26</sup> and  $\text{H}_2$ . This unanticipated reactivity introduced the possibility of converting **1-M** into **2-M** *via* cross-dehydrocoupling of the former with  $\text{MesSbH}_2$ ; in the case of **2-Y**, the reaction is quantitative by  $^1\text{H}$  NMR spectroscopy (Fig. S5†), and for **2-Dy** the isolated yield was 45%. The dehydrocoupling reactivity is considered further after discussion of the structural and magnetic properties of **1-Dy** and **2-Dy**.

The structures of **1-M** and **2-M** were determined by X-ray diffraction (Fig. 1, Tables S1 and S2†). Each compound contains a chair-like  $\text{M}_3\text{Sb}_3$  ring in which the metal atoms bond to two

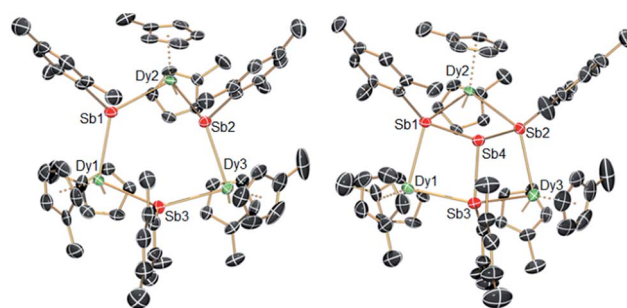


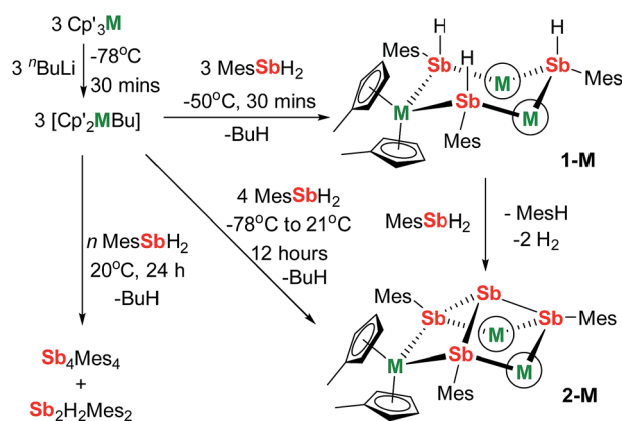
Fig. 1 Molecular structures of **1-Dy** (left) and **2-Dy** (right). Thermal ellipsoids at the 50% probability level. Hydrogen atoms not shown.

$\mu\text{-}[\text{Mes}(\text{H})\text{Sb}]^-$  ligands in **1-M** or to two antimony atoms of the  $[\text{Sb}_4\text{Mes}_3]^{3-}$  ligand in **2-M**. The metal atoms also bond to two  $\eta^5\text{-Cp}'$  ligands, such that they adopt pseudo-tetrahedral geometries. The central antimony atom in **2-M** connects the three  $\mu\text{-}[\text{MesSb}]$  groups, with Sb–Sb distances of 2.8583(11)–2.8687(11) Å in **2-Dy**. The  $\text{Dy}_3\text{Sb}_3$  rings in both dysprosium compounds are similar in size, with the Dy–Sb bond lengths in **1-Dy** being 3.092(6)–3.212(3) Å, and those in **2-Dy** 3.119(1)–3.138(1) Å. The Dy···Dy separations are 5.7174(7)–5.8535(5) Å and 5.7175(8)–5.8293(8) Å in **1-Dy** and **2-Dy**, respectively. The Sb–Dy–Sb angles are 87.53(8)–103.85(12) $^\circ$  in **1-Dy** and 85.32(3)–89.15(3) $^\circ$  in **2-Dy**; the Dy–Sb–Dy angles are 128.26(3)–136.73(14) $^\circ$  and 132.03(3)–136.96(3) $^\circ$ , respectively. The Dy–C distances in **1-Dy** and **2-Dy** are 2.59(1)–2.651(9) Å and 2.58(1)–2.66(1) Å, and the  $\text{Cp}_{\text{cent}}\text{-Dy-Cp}_{\text{cent}}$  angles are 129.30(17)–130.92(19) $^\circ$  and 129.9(2)–130.3(2) $^\circ$ . The geometric parameters for **1-Y** and **2-Y** are similar to those of their dysprosium analogues (Fig. S2 and Table S2†). The  $C_1$  symmetry of **1-Y** and **2-Y** in the solid state is reflected in their  $^1\text{H}$  NMR spectra, which show multiple resonances for the inequivalent CH and  $\text{CH}_3$  groups in both molecules (Fig. S3 and S4†). Characteristic Sb–H stretches were observed in the IR spectra of **1-M** at 1860–1875  $\text{cm}^{-1}$  (Fig. S6†).

Molecular rare-earth complexes of antimony ligands are extremely rare. The sole prior example of a Zintl-ligated rare-earth complex is  $[(\text{Cp}^*_2\text{Sm})_3(\text{Sb}_3)]$ , which contains the chain-like  $[\text{Sb}_3]^{3-}$  ligand.<sup>27</sup> The  $[\text{Sb}_4\text{R}_3]^{3-}$  ligand motif is itself extremely rare, with the only previous example being found in  $[(\text{Cp}_2\text{Ti})_3\{(\text{SbR})_3\text{Sb}\}]$ , which forms in the reaction of  $[\text{Cp}_2\text{Ti}\{\text{C}_2(\text{SiMe}_3)_2\}]$  with  $\text{Sb}_2\text{R}_4$  ( $\text{R} = 2\text{-(Me}_2\text{NCH}_2)_2\text{C}_6\text{H}_4$ ).<sup>28</sup>

### Magnetic properties

The magnetic susceptibilities of **1-Dy** and **2-Dy** were measured in a d.c. field of 1 kOe. The plots of  $\chi_{\text{M}}T(T)$  in the range 2–300 K for both compounds are similar (Fig. S7†) and consistent with the presence of three  $\text{Dy}^{3+}$  ions with  $^6\text{H}_{15/2}$  ground terms and  $g_f = 4/3$  (theoretical  $\chi_{\text{M}}T = 42.5 \text{ cm}^3 \text{ K mol}^{-1}$  at 300 K). For **1-Dy**,  $\chi_{\text{M}}T$  is  $40.57 \text{ cm}^3 \text{ K mol}^{-1}$  at 300 K before gradually decreasing upon cooling to 50 K; at lower temperatures the decrease in  $\chi_{\text{M}}T$  is more rapid, reaching  $10.01 \text{ cm}^3 \text{ K mol}^{-1}$  at 2 K. The values of  $\chi_{\text{M}}T$  for **2-Dy** at 300 K and 2 K are  $42.69 \text{ cm}^3 \text{ K mol}^{-1}$  and  $10.10 \text{ cm}^3 \text{ K mol}^{-1}$ , respectively. The field ( $H$ ) dependence of the magnetization ( $M$ ) at 1.8 K is also similar for **1-Dy** and **2-Dy**, with



Scheme 1 Synthesis of **1-M** and **2-M** (M = Dy, Y; Mes = mesityl; the circled M represents  $\text{Cp}'_2\text{M}$ ).



both showing a steep increase in  $M$  as the field increases to 20 kOe, and then a slower increase, before reaching  $15.17 \mu_B$  and  $15.82 \mu_B$ , respectively, at 70 kOe (Fig. S8†).

Comparing the experimental and calculated magnetic properties for **1-Dy** and **2-Dy** in the absence of intramolecular exchange interactions, it is clear that the experimental decrease in  $\chi_M T$  at low temperatures cannot be due to ligand field effects alone. Similarly, the increase in magnetization at low fields is slower than calculated. These observations imply non-negligible antiferromagnetic exchange interactions between the dysprosium centres, which were simulated by implementing the Lines model<sup>29,30</sup> and the Hamiltonian shown in eqn (1) using PHI.<sup>31</sup>

$$\hat{H} = \sum_{i=1}^3 \sum_{k=2,4,6} \sum_{q=-k}^k B_{k_i}^q \hat{O}_{k_i}^q + \mu_B g_J \sum_{i=1}^3 \vec{J}_i \cdot \vec{B} - 2J_{\text{iso}} \left( \vec{S}_1 \cdot \vec{S}_2 + \vec{S}_2 \cdot \vec{S}_3 + \vec{S}_3 \cdot \vec{S}_1 \right) \quad (1)$$

Here, the  $\hat{O}_{k_i}^q$  operator equivalents act on the  $|J, m_J\rangle_i$  basis of the  ${}^6\text{H}_{15/2}$  term of each  $\text{Dy}^{3+}$  ion where the  $B_{k_i}^q$  crystal field terms are fixed from CASSCF calculations (see below) taking into account the relative orientations of the local reference frames of each  $\text{Dy}^{3+}$  ion. The only variable is the single isotropic Lines exchange constant  $J_{\text{iso}}$ , which acts on the true  $S = 5/2$  spins of the  $\text{Dy}^{3+}$  ions *via* a Clebsch–Gordan decoupling; we use this term to account for both the exchange and dipolar coupling. Modelling the interactions in this way, the best simulations are obtained for **1-Dy** and **2-Dy** using  $J_{\text{iso}} = -0.121 \text{ cm}^{-1}$  and  $-0.150 \text{ cm}^{-1}$ , respectively (Fig. S7 and S8†).

The SMM properties of **1-Dy** and **2-Dy** were investigated using a.c. magnetic susceptibility measurements, employing a weak a.c. field of 1.55 Oe and zero d.c. field. In order to explore the impact of exchange interactions on the SMM properties, we also studied the magnetically dilute analogues  $[(\text{Cp}'_2\text{Dy})(\text{Cp}'_2\text{Y})_2\text{-}\{\text{Sb}(\text{H})\text{Mes}\}_3]$  (**Dy@1-Y**) and  $[(\text{Cp}'_2\text{Dy})(\text{Cp}'_2\text{Y})_2\{\text{Sb}(\text{Mes})_3\text{Sb}\}]$  (**Dy@2-Y**). Dilution levels of 5% were achieved by combining  $\text{Cp}'_3\text{Y}$  and  $\text{Cp}'_3\text{Dy}$  in 19 : 1 ratio and performing the syntheses according to Scheme 1, which produced **Dy@1-Y** and **Dy@2-Y** in matrices of **1-Y** and **2-Y**, respectively. The frequency ( $\nu$ ) dependence of the in-phase ( $\chi'$ ) (Fig. S9 and S10†) and the out-of-phase ( $\chi''$ ) (Fig. 2) magnetic susceptibilities reveal prominent SMM behaviour for **1-Dy** and **2-Dy**. The  $\chi''(\nu)$  plots for both systems show well-defined maxima in the temperature range 5–36 K and 4–33 K, respectively, using a.c. frequencies up to 1400 Hz. The plots of  $\chi''$  vs.  $\chi'$  for the undiluted SMMs are semi-circular in nature, and were fitted using a modified Debye model with  $\alpha$  parameters of 0.20–0.52 and 0.19–0.40 for **1-Dy** and **2-Dy**, respectively, indicating broad distributions of relaxation times (Fig. S11†). The diluted systems **Dy@1-Y** and **Dy@2-Y** also show pronounced SMM behaviour, with maxima in  $\chi''(\nu)$  being observed up to slightly higher temperatures relative to the undiluted SMMs (Fig. 2, S12 and S13†). The  $\alpha$  parameters for the dilute SMMs are 0.25–0.44 and 0.03–0.43 for **Dy@1-Y** and **Dy@2-Y**, respectively (Fig. S14†).

Insight into the relaxation dynamics of the SMMs was obtained by plotting  $\ln \tau$  versus  $T^{-1}$  (Fig. 2), where  $\tau$  is the

relaxation time. The four SMMs display similar properties, where the high-temperature regimes show a linear dependence of  $\ln \tau$  on  $T^{-1}$ , indicating relaxation *via* Orbach and/or thermally assisted quantum tunnelling of the magnetization (TA-QTM) mechanisms. At lower temperatures, the relaxation shows a weaker temperature dependence, suggesting relaxation *via* a Raman process; as the experiment was conducted in zero field, relaxation *via* the direct process is expected to be negligible. Notably, the relaxation dynamics do not enter a temperature-independent regime (usually assigned to ground-state QTM) at the lowest temperatures attainable by our SQUID magnetometer. The data was modelled for each SMM using the equation  $\tau^{-1} = \tau_0^{-1} e^{-U_{\text{eff}}/k_B T} + CT^n$ , where  $\tau_0$  and  $U_{\text{eff}}$  are the Orbach parameters, and  $C$  and  $n$  are the Raman parameters (Table 1). The  $U_{\text{eff}}$  value of  $345 \text{ cm}^{-1}$  for **1-Dy** is one of the largest yet determined for a polycrystalline SMM in zero applied field. The highest anisotropy barriers in SMMs based on lanthanide ions with oblate electron density in the most magnetic  $m_J$  states – such as  $\text{Dy}^{3+}$  – typically occur when strong crystal fields are applied on high-order symmetry axes.<sup>8</sup> Thus, the current record anisotropy barrier is  $1261 \text{ cm}^{-1}$ , which was determined for a  $D_{5h}$ -symmetric dysprosium complex with a pentagonal bipyramidal arrangement of donor atoms.<sup>21</sup> In light of this, a remarkable observation on **1-Dy** is that a very large barrier can still be obtained when the  $\text{Dy}^{3+}$  occupies a much lower symmetry environment of approximately  $C_{2v}$  (assuming ring whizzing of the  $\text{Cp}'$  ligands). The Raman exponents  $n$  are similar to those in other metallocene-based SMMs.<sup>32</sup>

Variable-field magnetization measurements on the SMMs revealed marked differences between the non-dilute and dilute systems. For **1-Dy**, a sweep rate of  $2 \text{ mT s}^{-1}$  produced a narrow S-shaped hysteresis loop at 1.8 K (Fig. S15†), whereas butterfly-shaped loops were observed for **Dy@1-Y** at 1.8–5.4 K (Fig. 2). The hysteresis properties of **2-Dy** and **Dy@2-Y** (Fig. 2 and S15†) mirror those of the stibine-ligated compounds, albeit with the  $M(H)$  loops for the diluted system remaining open up to 4.0 K. The likeliest explanation for the closed hysteresis loops in the non-dilute SMMs is that exchange interactions between the  $\text{Dy}^{3+}$  ions provide tunnelling pathways that close upon replacement with diamagnetic  $\text{Y}^{3+}$ . The precipitous drop in magnetization for the diluted SMMs around zero field is characteristic of the vast majority of SMMs and can be attributed to single-ion effects such as hyperfine coupling to spin-active isotopes of dysprosium.<sup>33</sup>

### Theoretical characterization

Deeper insight into the magnetic properties of **1-Dy** and **2-Dy** was obtained by performing complete active space self-consistent field (CASSCF) calculations.<sup>34</sup> For both complexes, the electronic structure of the individual  $\text{Dy}^{3+}$  ions is dominated by the  $[\text{Cp}']^-$  ligands, which creates a strong axial potential and leads to the ground Kramers doublet at each  $\text{Dy}^{3+}$  ion being well described as  $m_J = \pm 15/2$ . The main magnetic anisotropy axis of each  $\text{Dy}^{3+}$  ion is therefore oriented along the local  $[\text{Cp}'] \cdots [\text{Cp}']$  direction, where all three form a teepee-like arrangement (Fig. 3). The dominant axial potential generated by the  $[\text{Cp}']^-$  ligands also results in the first- and second-excited states being



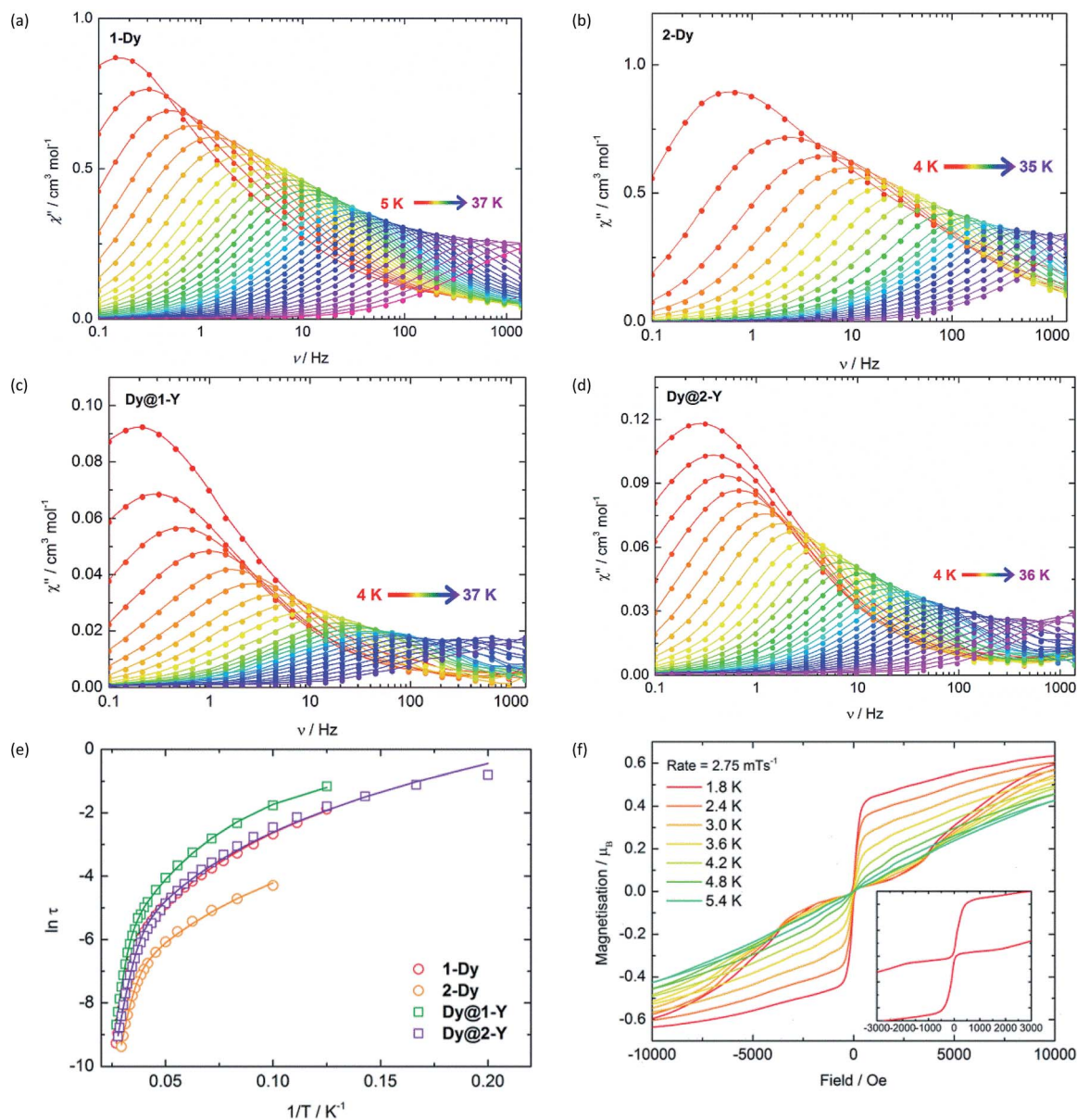


Fig. 2 Frequency dependence of the out-of-phase ( $\chi''$ ) magnetic susceptibility for: (a) 1-Dy; (b) 2-Dy; (c) Dy@1-Y; (d) Dy@2-Y. (e) Temperature dependence of the magnetization relaxation times ( $\tau$ ) plotted as  $\ln(\tau/s)$  vs.  $T^{-1}$ , with the solid lines representing theoretical fits using the parameters in Table 1. (f) Magnetization ( $M$ ) vs. field ( $H$ ) hysteresis loops for Dy@1-Y with a scan rate of  $2.8 \text{ mT s}^{-1}$ .

Table 1 Parameters used to fit the magnetization dynamics of 1-Dy, Dy@1-Y, 2-Dy and Dy@2-Y

|                                 | 1-Dy                   | Dy@1-Y                 | 2-Dy                  | Dy@2-Y                |
|---------------------------------|------------------------|------------------------|-----------------------|-----------------------|
| $U_{\text{eff}}/\text{cm}^{-1}$ | 345                    | 345                    | 272                   | 270                   |
| $\tau_0/s$                      | $1.57 \times 10^{-10}$ | $2.96 \times 10^{-10}$ | $1.10 \times 10^{-9}$ | $2.87 \times 10^{-9}$ |
| $C/s^{-1} \text{K}^{-n}$        | $6.15 \times 10^{-3}$  | $2.57 \times 10^{-3}$  | 0.128                 | $6.36 \times 10^{-3}$ |
| $n$                             | 3.35                   | 3.39                   | 2.72                  | 3.30                  |

highly axial in nature and collinear with the ground-state axis for all sites in 1-Dy and 2-Dy (Tables 2 and S3–S8†).

The  $C_{2v}$  symmetry of the dysprosium environments renders a rhombic third excited state in both complexes; this is likely to

be the origin of the most efficient thermal relaxation pathway in 1-Dy since the rhombic state is calculated to lie at  $416(3) \text{ cm}^{-1}$ , which is comparable to the experimental  $U_{\text{eff}}$  value of  $345 \text{ cm}^{-1}$ . For 2-Dy, the rhombic third excited state lies at  $413(17) \text{ cm}^{-1}$ , which is much larger than the experimental barrier of  $270 \text{ cm}^{-1}$ . Although relaxation *via* higher-lying Kramers' doublets is known,<sup>35–37</sup> it remains a relatively uncommon phenomenon, with thermally activated relaxation thought to proceed *via* the first-excited doublet in most SMMs.<sup>38</sup> In both cases, magnetic dilution does not significantly alter the a.c. susceptibility properties, hence the discrepancy between theory and experiment for 2-Dy cannot arise from intramolecular interactions. Despite the differing ligand environments in 1-Dy and 2-Dy, the properties of the low-lying Kramers doublets in both complexes



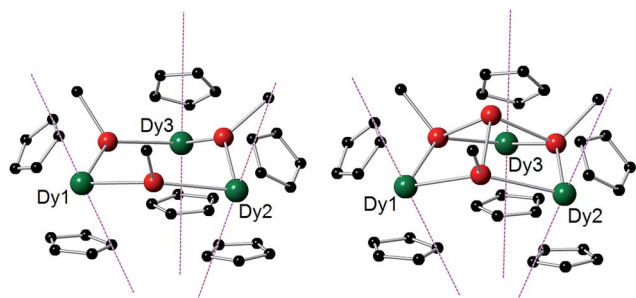


Fig. 3 Orientations of the main magnetic axes for the ground doublets of the  $\text{Dy}^{3+}$  ions in **1-Dy** (left) and **2-Dy** (right). The magnetic axes are shown as dashed purple lines. Dy = green, Sb = red, C = black. For clarity, only the *ipso* carbons of the mesityl substituents are shown, and the  $\text{Cp}'$  methyl groups and hydrogen atoms have been omitted.

Table 2 Properties of the four lowest-energy Kramers doublets in **1-Dy** and **2-Dy**. Energies and  $g$ -tensor values are averaged across the three  $\text{Dy}^{3+}$  sites in each molecule. Standard deviations are given in brackets. 'Angle' refers to the orientation of the magnetic axis relative to that in the ground doublet

| Doublet     | Energy/ $\text{cm}^{-1}$ | $g_x$   | $g_y$   | $g_z$    | Angle/ $^\circ$ |
|-------------|--------------------------|---------|---------|----------|-----------------|
| <b>1-Dy</b> |                          |         |         |          |                 |
| 1           | 0                        | 0.00    | 0.00    | 19.57(5) |                 |
| 2           | 167(3)                   | 0.00    | 0.00    | 17.04(7) | 2.6(7)          |
| 3           | 329(5)                   | 0.04(3) | 0.05(3) | 14.74(3) | 3.5(9)          |
| 4           | 416(3)                   | 2(1)    | 4(3)    | 11(1)    | 24(33)          |
| <b>2-Dy</b> |                          |         |         |          |                 |
| 1           | 0                        | 0.00    | 0.00    | 19.66(1) |                 |
| 2           | 166(1)                   | 0.00    | 0.00    | 17.12(3) | 3.0(5)          |
| 3           | 324(9)                   | 0.03(2) | 0.04(3) | 14.69(5) | 1.6(5)          |
| 4           | 417(13)                  | 0.6(3)  | 0.7(3)  | 11.6(2)  | 3.9(7)          |

are remarkably similar, as are the orientations of the ground-state anisotropy axes. The LoProp charges on the antimony atoms bonded to the  $\text{Dy}^{3+}$  centres range from  $-0.17$  to  $-0.23$  for **1-Dy** and from  $-0.28$  to  $-0.29$  for **2-Dy**, respectively.<sup>39</sup> Although the accumulation of charge on the donor atoms is not large in either case, the negligible difference in the average Dy–Sb bond lengths of  $0.036 \text{ \AA}$  between the two systems combined with the slightly greater charge density on the antimony atoms in the equatorial plane in **2-Dy** relative to **1-Dy** can account for the lower  $U_{\text{eff}}$  value in the former, which is consistent with observations on related SMMs containing  $[\text{MesE}(\text{H})]^-$  and  $[\text{MesE}]^{2-}$  ligands ( $\text{E} = \text{P}, \text{As}$ ).<sup>40,41</sup> The  $U_{\text{eff}}$  value determined for **1-Dy** of  $345 \text{ cm}^{-1}$  is markedly larger than those determined for the isostructural phosphide- and arsenide-bridged analogues  $[(\eta^5\text{-Cp}'_2\text{Dy})\{\mu\text{-E}(\text{H})\text{Mes}\}]_3$  ( $\text{E} = \text{P}, \text{As}$ ), of  $210 \text{ cm}^{-1}$  and  $256 \text{ cm}^{-1}$ , respectively. The only significant differences in the molecular structures of **1-Dy** and the two lighter congeners are the dysprosium–pnictogen bond lengths, which increase significantly with the radius of pnictogen (those in **1-Dy** are, on average,  $0.168 \text{ \AA}$  longer than those in the As-bridged analogue). Since the main magnetic axes in the phosphide-, arsenide- and stibinide-bridged SMMs all adopt similar orientations along the

$[\text{Cp}']\cdots[\text{Cp}']$  directions, the pnictogens occupy equatorial sites; as the Dy–E bond lengths increase, the influence of the pnictogen on the splitting of the  $\text{Dy}^{3+}$  crystal field levels diminishes, leading to a more dominant axial crystal field and hence larger  $U_{\text{eff}}$  values.

Being intrigued by the unusual  $[\text{Sb}_4\text{Mes}_4]^{3-}$  ligand, we endeavoured to determine the electronic structure of this species. The  $\text{Dy}^{3+}$  ions in **2-Dy** were replaced with  $\text{Lu}^{3+}$  to ensure a well-defined active space for the antimony-containing ligand, and the restricted active space (RAS) probing approach was employed with **2-Lu** to identify an appropriate orbital manifold near the Fermi level to describe the  $\text{Sb}_4$  unit. The resulting CAS, which consisted of 12 electrons in 9 orbitals for the lowest lying ten  $S = 0$  and ten  $S = 1$  states delocalized over the  $\text{Sb}_4$  unit, is dominated by the antimony 5p orbitals (Fig. S16†). The ground state of  $[\text{Sb}_4\text{Mes}_4]^{3-}$  is a well-isolated  $S = 0$ , as expected, however after the first excitation to the  $S = 1$  state at *ca.*  $26\,000 \text{ cm}^{-1}$ , there is a continuum of states up to at least  $45\,000 \text{ cm}^{-1}$  (Table S9 and Fig. S17†). This delocalized set of continuum states is reminiscent of a semi-conductor, and it is possible that this feature also contributes to diminishing  $U_{\text{eff}}$  in **2-Dy**. Unfortunately, however, all efforts to calculate the properties of the individual  $\text{Dy}^{3+}$  ions while allowing excitation into the  $\text{Sb}_4$  continuum failed owing to the extremely large active space required for the calculation.

### Stibine dehydrocoupling reactivity

In optimizing the synthesis of **1-M** and **2-M**, it was apparent from  $^1\text{H}$  NMR spectroscopic studies of the yttrium derivatives that **1-Y**, **2-Y**,  $\text{Sb}_2\text{H}_2\text{Mes}_2$ ,  $\text{Sb}_4\text{Mes}_4$  and  $\text{H}_2$  all form during the same reaction. Furthermore, the relative amounts of each component depend on reaction time and temperature, with longer times and higher temperatures producing greater amounts of  $\text{Sb}_4\text{Mes}_4$ . These observations implied that yttrium mediates – or even catalyses – the dehydrocoupling of  $\text{MesSbH}_2$ . To investigate this possibility,  $^1\text{H}$  NMR spectroscopy was used to study the reactions of  $\text{MesSbH}_2$  with 10 mol% of  $\text{Cp}'_3\text{Y}$  at 40, 50, 60 and  $70 \text{ }^\circ\text{C}$  (Fig. S18–S21†). The initial  $^1\text{H}$  NMR spectrum of the  $40 \text{ }^\circ\text{C}$  reaction shows the resonances of the two starting materials (Fig. S18†), whereas after 20 hours  $\text{MesSbH}_2$ ,  $\text{Sb}_2\text{H}_2\text{Mes}_2$  (both diastereomers) and  $\text{Sb}_4\text{Mes}_4$ , account for 40%, 43% and 17% of the antimony-containing species (Fig. 4). The  $^1\text{H}$  NMR spectrum also shows  $\text{H}_2$  at 4.47 ppm. The amount of  $\text{Sb}_2\text{H}_2\text{Mes}_2$  then gradually decreases, accounting for 20% after 170 h, whereas the amount of  $\text{Sb}_4\text{Mes}_4$  increases to reach 71%, with 7%  $\text{MesSbH}_2$  remaining. Also noteworthy in the  $^1\text{H}$  NMR spectrum is the rapid emergence of a series of broad resonances in the region  $\delta \approx 6.1\text{--}6.6 \text{ ppm}$ , which correspond to the methine CH resonances of **1-Y**. After 170 h, all the signals due to **1-Y** have been replaced by those of **2-Y**. At  $50 \text{ }^\circ\text{C}$ , the conversion of  $\text{MesSbH}_2$  to  $\text{Mes}_4\text{Sb}_4$  increases to 80% at a faster rate, but at higher temperatures the conversion level decreases and, at  $70 \text{ }^\circ\text{C}$ , an appreciable amount of mesitylene was observed due to decomposition of  $\text{MesSbH}_2$  (Fig. S22†). Thus,  $\text{Cp}'_3\text{Y}$  does catalyse the dehydrocoupling of  $\text{MesSbH}_2$  to give  $\text{Sb}_2\text{H}_2\text{Mes}_2$  and then  $\text{Sb}_4\text{Mes}_4$ .



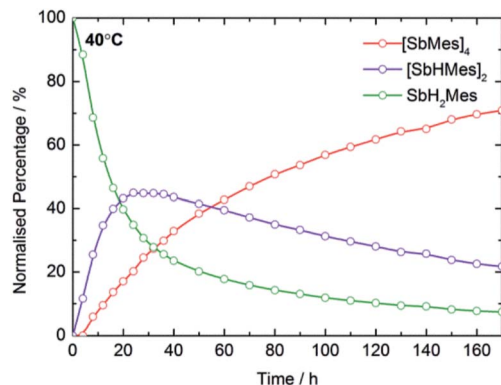
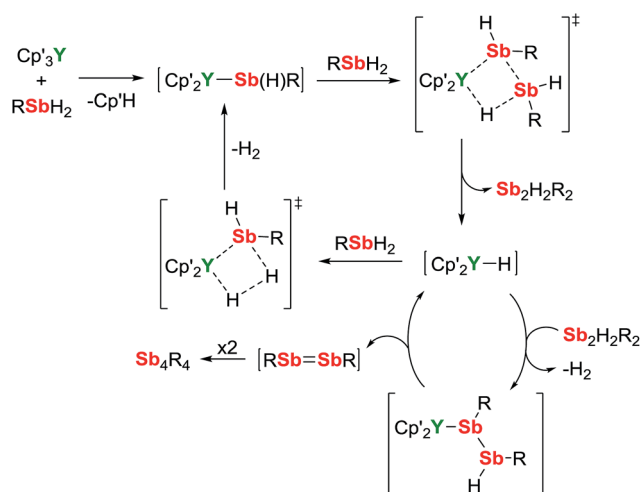


Fig. 4 Product distribution as a function of time at 40 °C for the dehydrocoupling of MesSbH<sub>2</sub> initiated by 10 mol% Cp'<sub>3</sub>Y.

The initial yttrium-containing product of the dehydrocoupling is **1-Y**, which is subsequently converted into **2-Y**. Since our stoichiometric (Scheme 1) and catalytic reaction studies have established that **1-Y** reacts quantitatively with MesSbH<sub>2</sub> to give **2-Y** (Fig. S5†), the fate of **2-Y** once formed is of interest. This was probed by adding 3.33 mol% of **2-Y** (*i.e.* 10 mol% yttrium) to MesSbH<sub>2</sub> and following the reaction by <sup>1</sup>H NMR spectroscopy at 40 °C (Fig. S23†). The resulting spectra acquired over 345 h reveal that, although the reaction is slower than with Cp'<sub>3</sub>Y as the catalyst, **2-Y** does dehydrocouple MesSbH<sub>2</sub> to give Sb<sub>2</sub>H<sub>2</sub>Mes<sub>2</sub> and H<sub>2</sub>, and then Sb<sub>4</sub>Mes<sub>4</sub>.

A mechanism for the catalytic dehydrocoupling of MesSbH<sub>2</sub> by Cp'<sub>3</sub>Y is proposed in Scheme 2. The variation in the relative amounts of MesSbH<sub>2</sub>, Sb<sub>2</sub>H<sub>2</sub>Mes<sub>2</sub> and Sb<sub>4</sub>Mes<sub>4</sub> as a function of time, in addition to the formation of H<sub>2</sub>, suggests: (i) that the distibine is formed from dehydrocoupling of MesSbH<sub>2</sub>, and; (ii) that the tetrastibetane is formed subsequently from further reactivity of the distibine. The formation of Sb<sub>2</sub>H<sub>2</sub>Mes<sub>2</sub> also implies that the dehydrocoupling does not occur *via* stibinidene (*i.e.* RSb) elimination, which would only produce cyclic oligomers of the type [MesSb]<sub>*n*</sub>. Thus, we envisage deprotonation of

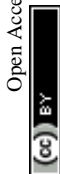


Scheme 2 Dehydrocoupling of MesSbH<sub>2</sub> catalysed by Cp'<sub>3</sub>Y (R = mesityl).

MesSbH<sub>2</sub> by Cp'<sub>3</sub>Y, which acts as a pre-catalyst, leading to the putative stibinide complex [Cp'<sub>2</sub>YSb(H)Mes], *i.e.* the monomeric unit of the trimer **1-Y**. Addition of a second equivalent of MesSbH<sub>2</sub> can lead to the formation of a cyclic, four-membered transition state in which the distibine Sb<sub>2</sub>H<sub>2</sub>Mes<sub>2</sub> forms, thus generating a hydride-ligated intermediate [Cp'<sub>2</sub>YH]. A second four-membered transition state can then be proposed from which [Cp'<sub>2</sub>YSb(H)Mes] is re-formed along with elimination of dihydrogen. The proposed  $\sigma$ -bond metathesis transition states in Scheme 2 are consistent with those thought to occur in several different types of dehydrocoupling reactions catalysed by main group and transition metal complexes.<sup>42</sup> To account for the formation of Sb<sub>4</sub>Mes<sub>4</sub> from Sb<sub>2</sub>H<sub>2</sub>Mes<sub>2</sub>, we propose a mechanism in which the distibine is deprotonated by [Cp'<sub>2</sub>YH] to give an intermediate distibinide complex [Cp'<sub>2</sub>Y{RSb-Sb(H)R}], which subsequently undergoes a  $\beta$ -hydride elimination to regenerate the yttrium hydride and form the distibene MesSb=SbMes. Since heavy p-block analogues of alkenes tend to cyclo-oligomerize owing to the weak nature of the multiple bonds,<sup>43</sup> the formation of Sb<sub>4</sub>Mes<sub>4</sub> can be accounted for by dimerization of the distibene.

Dehydrocoupling catalysis has emerged as one of the most important methods for the synthesis of homo- or hetero-nuclear bonds between p-block elements.<sup>44</sup> Considerable attention has focused on the synthesis of inorganic polymers, especially poly(ammonia-borane) and poly(amine-boranes), owing to their proposed applications as hydrogen storage and delivery materials.<sup>45</sup> Notably, only one example of metal-catalysed stibine dehydrocoupling has previously been reported, which employed the group 4 metallocenes [(Cp\*)(Cp)M(H)Cl] (M = Zr, Hf) as catalysts at 5 mol% loading for the formation of Sb<sub>4</sub>Mes<sub>4</sub> from MesSbH<sub>2</sub>.<sup>46</sup> This reaction is thought to proceed *via* a mechanism that involves  $\alpha$ -elimination of highly reactive stibinidene (SbR) fragments, which subsequently cyclo-oligomerize to Sb<sub>*n*</sub>R<sub>*n*</sub>. Many catalysts based on main group metals and transition metals are well established for the dehydrocoupling of a range of element–element bonds,<sup>42,44</sup> however surprisingly few examples employ rare earth elements. A recent study has shown that divalent rare earth alkyl complexes are effective catalysts for the cross-dehydrocoupling of silanes and amines to give silazanes.<sup>47</sup>

The cross-dehydrocoupling of **1-Dy** with mesitylstibine to give **2-Dy** is the first example of such reactivity being used to synthesize an SMM. Our observations therefore represent a new catalytic transformation in rare-earth chemistry and a new synthetic strategy in molecular magnetism. The observation of SMM behaviour for **1-Dy**, **2-Dy** and their magnetically dilute analogues in light of the role of **1-Y** and **2-Y** in stibine dehydrocoupling is also significant. Although the paramagnetism of the dysprosium systems precludes detailed study by NMR spectroscopy, crystalline Sb<sub>2</sub>H<sub>2</sub>Mes<sub>2</sub>, Sb<sub>4</sub>Mes<sub>4</sub> can be isolated from the dehydrocoupling of MesSbH<sub>2</sub> catalysed by 10 mol% Cp'<sub>3</sub>Dy. In light of the similar chemistry of Y<sup>3+</sup> and Dy<sup>3+</sup>, **1-Dy** and **2-Dy** should therefore also be intermediates in the catalytic stibine dehydrocoupling. Thus, the dysprosium–antimony compounds display two functions that can be accessed by varying the temperature, since cooling **1-Dy** and **2-Dy** below 40 K



leads to SMM behaviour, and heating them in solution above 313 K results in catalytic stibine dehydrocoupling.

## Conclusions

In summary we have synthesized the first antimony-ligated SMMs. The anisotropy barriers of **1-Dy**, **2-Dy** in zero applied field, and of their diluted analogues, are  $U_{\text{eff}} = 345 \text{ cm}^{-1}$  and  $270 \text{ cm}^{-1}$ , respectively, placing them amongst the highest yet reported. The conversion of **1-Dy** into **2-Dy** via cross dehydrocoupling with mesitylstibine represents a novel synthetic strategy in molecular magnetism. Indeed, our initial aim of targeting SMMs with lanthanide–metalloid bonds has resulted in the identification new catalytic reactivity for the rare earth elements. Given the broad scope of dehydrocoupling chemistry, the synthetic strategy has considerable potential to be extended to incorporate many new and unconventional chemical environments into molecular magnets. The next challenge is to extend the reactivity to synthesize SMMs that can be regarded as molecular alloys, *i.e.* systems in which the magnetic centres are bonded to the heaviest stable metallic elements. Based on the periodic trend in the anisotropy barrier unearthed during this study, *i.e.* that  $U_{\text{eff}}$  tends to increase with increasing radius of the pnictogen, substantial increases in  $U_{\text{eff}}$  can be expected for SMMs ligated by the 6p elements thallium, lead and bismuth, provided the chemical environments can be stabilized. Ongoing work in our laboratory will pursue these targets.

## Acknowledgements

R.A.L. thanks the European Research Council for the Consolidator Grant 'RadMag' (646740), and also the EPSRC for an Early Career Fellowship (grant EP/M022064/1). N.F.C. thanks the Ramsay Memorial Trust for a Research Fellowship. The authors acknowledge the EPSRC UK National Electron Paramagnetic Resonance Facility and Service at The University of Manchester for access to the SQUID magnetometer.

## Notes and references

- M. S. Fataftah, J. M. Zadrozny, S. C. Coste, M. J. Graham, D. M. Rogers and D. E. Freedman, *J. Am. Chem. Soc.*, 2016, **138**, 1344.
- Y.-Z. Zheng, G.-J. Zhou, Z. Zheng and R. E. P. Winpenny, *Chem. Soc. Rev.*, 2014, **43**, 1462.
- S. Brooker, *Chem. Soc. Rev.*, 2015, **44**, 2880.
- A. Bousseksou, G. Molnár, L. Salmon and W. Nicolazzi, *Chem. Soc. Rev.*, 2011, **40**, 3313.
- O. A. Blackburn, A. M. Kenwright, A. R. Jupp, J. M. Goicoechea, P. D. Beer and S. Faulkner, *Chem.–Eur. J.*, 2016, **22**, 8929.
- W.-M. Liu, P. H. J. Keizers, M. A. S. Hass, A. Blok, M. Timmer, A. J. C. Sarris, M. Overhand and M. Ubbink, *J. Am. Chem. Soc.*, 2012, **134**, 17306.
- C. Shen and E. J. New, *Curr. Opin. Chem. Biol.*, 2013, **17**, 158.
- D. N. Woodruff, R. E. P. Winpenny and R. A. Layfield, *Chem. Rev.*, 2013, **113**, 5110.
- C. Papatriantafyllopoulou, E. E. Moushi, G. Christou and A. J. Tasiopoulos, *Chem. Soc. Rev.*, 2016, **45**, 1597.
- D. Gatteschi, R. Sessoli and J. Villain, *Molecular Nanomagnets*, Oxford University Press, Oxford, 2006.
- J. M. Frost, K. L. M. Harriman and M. Murugesu, *Chem. Sci.*, 2016, **7**, 2470.
- J. M. Zadrozny, D. J. Xiao, M. Atanasov, G. J. Long, F. Grandjean, F. Neese and J. R. Long, *Nat. Chem.*, 2013, **5**, 577.
- R. A. Layfield, *Organometallics*, 2014, **33**, 1084.
- N. Ishikawa, M. Sugita, T. Ishikawa, S. Koshihara and Y. Kaizu, *J. Am. Chem. Soc.*, 2003, **125**, 8694.
- (a) M. A. Aldamen, J. M. Clemente-Juan, E. Coronado, C. Martí-Gastaldo and A. Gaita-Ariño, *J. Am. Chem. Soc.*, 2008, **130**, 8874; (b) U. J. Williams, B. D. Mahoney, P. T. DeGregorio, P. J. Carroll, E. Nakamura-Ogiso, J. M. Kikkawa and E. J. Schelter, *Chem. Commun.*, 2012, **48**, 5593.
- P. Zhang, L. Zhang, C. Wang, S. F. Xue, S. Y. Lin and J. Tang, *J. Am. Chem. Soc.*, 2014, **136**, 4484.
- J. D. Rinehart, M. Fang, W. J. Evans and J. R. Long, *J. Am. Chem. Soc.*, 2011, **133**, 14236.
- R. A. Layfield, J. J. W. McDouall, S. A. Sulway, D. Collison, F. Tuna and R. E. P. Winpenny, *Chem.–Eur. J.*, 2010, **16**, 4442.
- P. Zhang, L. Zhang and J. Tang, *Dalton Trans.*, 2015, **44**, 3923.
- (a) Y.-C. Chen, J.-L. Liu, L. Ungur, J. Liu, Q.-W. Li, L.-F. Wang, Z.-P. Ni, L. F. Chibotaru, X.-M. Chen and M.-L. Tong, *J. Am. Chem. Soc.*, 2016, **138**, 2829; (b) J. Liu, Y.-C. Chen, J.-L. Liu, V. Vieru, L. Ungur, J.-H. Jia, L. F. Chibotaru, Y. Lan, W. Wernsdorfer, S. Gao, X.-M. Chen and M.-L. Tong, *J. Am. Chem. Soc.*, 2016, **138**, 5441.
- Y.-S. Ding, N. F. Chilton, R. E. P. Winpenny and Y.-Z. Zheng, *Angew. Chem., Int. Ed.*, 2016, DOI: 10.1002/anie.201609685.
- S. K. Gupta, T. Rajeshkumar, G. Rajaraman and R. Murugavel, *Chem. Sci.*, 2016, **7**, 5181.
- C. Cervetti, A. Rettori, M. G. Pini, A. Cornia, A. Repollé, F. Luis, M. Dressel, S. Rauschenbach, K. Kern, M. Burghard and L. Bogani, *Nat. Mater.*, 2016, **15**, 164.
- S. Thiele, F. Balestro, R. Ballou, S. Klyatskaya, M. Ruben and W. Wernsdorfer, *Science*, 2014, **344**, 1135.
- M. Ateş, H. J. Breunig, S. Güleç, W. Offermann, K. Häberle and M. Dräger, *Chem. Ber.*, 1989, **122**, 473.
- G. Balázs, H. J. Breunig, E. Lork and W. Offermann, *Organometallics*, 2001, **20**, 2666.
- W. J. Evans, S. L. Gonzales and J. W. Ziller, *J. Chem. Soc., Chem. Commun.*, 1992, 1138.
- H. J. Breunig, E. Lork, O. Moldovan, C. I. Rat, U. Rosenthal and C. Silvestru, *Dalton Trans.*, 2009, 5065.
- N. Iwahara and L. F. Chibotaru, *Phys. Rev. B: Condens. Matter Mater. Phys.*, 2015, **91**, 174438.
- M. E. Lines, *J. Chem. Phys.*, 1971, **55**, 2977.
- N. F. Chilton, R. P. Anderson, L. D. Turner, A. Soncini and K. S. Murray, *J. Comput. Chem.*, 2013, **34**, 1164.
- T. Pugh, N. F. Chilton and R. A. Layfield, *Angew. Chem., Int. Ed.*, 2016, **55**, 11082.



- 33 F. Pointillart, K. Bernot, S. Gohlen, B. Le Guennic, T. Guizouarn, L. Ouahab and O. Cador, *Angew. Chem., Int. Ed.*, 2015, **54**, 1504.
- 34 F. Aquilante, *et al.*, *J. Comput. Chem.*, 2016, **37**, 506.
- 35 (a) R. J. Blagg, L. Ungur, F. Tuna, J. Speak, P. Comar, D. Collison, W. Wernsdorfer, E. J. L. McInnes, L. F. Chibotaru and R. E. P. Winpenny, *Nat. Chem.*, 2013, **5**, 673; (b) Y. N. Guo, L. Ungur, G. E. Granroth, A. K. Powell, C. J. Wu, S. E. Nagler, J. Tang, L. F. Chibotaru and D. M. Cui, *Sci. Rep.*, 2014, **4**, 5471.
- 36 J. Wu, J. Jung, P. Zhang, H. Zhang, J. Tang and B. Le Guennic, *Chem. Sci.*, 2016, **7**, 3632.
- 37 I. Oyarzabal, J. Ruiz, E. Ruiz, D. Aravena, J. M. Seco and E. Colacio, *Chem. Commun.*, 2015, **51**, 12353.
- 38 J. P. Costes, C. Duhayon, S. Titos-Padilla, E. Colacio, I. Oyarzabal, T. Gupta and G. Rajaraman, *Inorg. Chem.*, 2016, **55**, 4428.
- 39 L. Gagliardi, R. Lindh and G. Karlström, *J. Chem. Phys.*, 2004, **121**, 4494.
- 40 T. Pugh, F. Tuna, L. Ungur, D. Collison, E. J. L. McInnes, L. F. Chibotaru and R. A. Layfield, *Nat. Commun.*, 2015, **6**, 7492.
- 41 T. Pugh, V. Vieru, L. F. Chibotaru and R. A. Layfield, *Chem. Sci.*, 2016, **7**, 2128.
- 42 E. M. Leitao, T. Jurca and I. Manners, *Nat. Chem.*, 2013, **5**, 817.
- 43 P. P. Power, *J. Chem. Soc., Dalton Trans.*, 1998, 2939.
- 44 R. Waterman, *Chem. Soc. Rev.*, 2013, **42**, 5629.
- 45 S. Bhunya, T. Malakar, G. Ganguly and A. Paul, *ACS Catal.*, 2016, **6**, 7907.
- 46 R. Waterman and T. D. Tilley, *Angew. Chem., Int. Ed.*, 2006, **45**, 2926.
- 47 A. Pindwal, A. Ellern and A. D. Sadow, *Organometallics*, 2016, **35**, 1674.

